catalysts

MDPI

Article

WS_2 as an Effective Noble-Metal Free Cocatalyst Modified $TiSi_2$ for Enhanced Photocatalytic Hydrogen Evolution under Visible Light Irradiation

Dongmei Chu [1], Chunyong Zhang [1], Ping Yang [1,*], Yukou Du [1] and Cheng Lu [2,*]

[1] College of Chemistry, Chemical Engineering and Materials Science, Soochow University, Suzhou 215123, China; dmchu2015@126.com (D.C.); zhangchunyong@126.com (C.Z.); duyk@suda.edu.cn (Y.D.)

[2] Department of Chemistry, University of Toronto, Toronto, ON M5S 3H6, Canada

* Correspondence: pyang@suda.edu.cn (P.Y.); clu@chem.utoronto.ca (C.L.); Tel./Fax: +86-512-6588-0089 (P.Y.); +1-416-978-4526 (C.L.)

Academic Editors: Di-Jia Liu and Jianguo Liu

Received: 23 July 2016; Accepted: 5 September 2016; Published: 10 September 2016

Abstract: A noble-metal free photocatalyst consisting of WS_2 and $TiSi_2$ being used for hydrogen evolution under visible light irradiation, has been successfully prepared by in-situ formation of WS_2 on the surface of $TiSi_2$ in a thermal reaction. The obtained samples were characterized by X-ray diffraction (XRD), scanning electron microscopy (SEM), energy dispersive X-ray spectrometry (EDX), transmission electron microscopy (TEM), and X-ray photoelectron spectroscopy (XPS). The results demonstrate that WS_2 moiety has been successfully deposited on the surface of $TiSi_2$ and some kind of chemical bonds, such as Ti-S-W and Si-S-W, might have formed on the interface of the $TiSi_2$ and WS_2 components. Optical and photoelectrochemical investigations reveal that $WS_2/TiSi_2$ composite possesses lower hydrogen evolution potential and enhanced photogenerated charge separation and transfer efficiency. Under 6 h of visible light ($\lambda > 420$ nm) irradiation, the total amount of hydrogen evolved from the optimal $WS_2/TiSi_2$ catalyst is 596.4 $\mu mol \cdot g^{-1}$, which is around 1.5 times higher than that of pure $TiSi_2$ under the same reaction conditions. This study shows a paradigm of developing the effective, scalable and inexpensive system for photocatalytic hydrogen generation.

Keywords: $WS_2/TiSi_2$ composite; noble-metal free; visible light; photocatalyst; hydrogen evolution

1. Introduction

Due to growing environmental concerns and increasing energy demands, hydrogen, as the highest energy density carrier per unit weight and an environmentally friendly energy source, has attracted great attention [1–6]. Since the discovery of hydrogen evolution through the photoelectrochemical water splitting on the TiO_2 electrode [7], photocatalytic water splitting to produce hydrogen under solar light irradiation has been considered as one of the most important approaches to meet the world energy demands and to solve environmental issues. However, TiO_2 as a photocatalyst for practical use is restricted by the low visible-light absorption and fast photogenerated electron-hole recombination [7–9]. To develop a novel, efficient, and cost-effective visible-light-driven photocatalyst is indispensable to realize the aim of applicable solar energy conversion [10–12].

Titanium disilicide ($TiSi_2$) is an excellent semiconductor material due to its high thermodynamic stability and excellent optical properties [13]. The band gap of $TiSi_2$ is in the range of 1.5 to 3.4 eV, suggesting that the absorption spectrum of $TiSi_2$ can cover almost the whole visible range and a part of the ultraviolet. The application of $TiSi_2$ for photocatalytic water splitting was first reported by Demuth et al. [14]. Using co-catalysts, such as RuO_2 and graphene, can further enhance the photocatalytic activity of $TiSi_2$-based catalyst, since electron-hole recombination is retarded [15].

As it is well known, the photocatalytic hydrogen production systems generally have two serious limitations: a high electron-hole recombination rate and a large hydrogen production overpotential [7–9]. In order to overcome these limitations, the most widely used approach is to use noble metal nanoparticles such as Pt as a co-catalyst [16–18]. However, high cost and a limited source of noble metals may have an adverse effect on the practical applications. Therefore, it is critical to develop a noble-metal free system for efficient photocatalytic hydrogen generation.

Transition-metal dichalcogenides, such as molybdenum disulphide (MoS_2) and tungsten disulphide (WS_2), have been used as co-catalysts and charge-transfer facilitators to improve the photocatalytic hydrogen production, owing to their graphene-like layered structure, high electron mobility, moderate bandgap, and rich active sites [19–23]. Since Guo's group first reported that WS_2 could efficiently improve the rate of H_2 evolution from TiO_2 under visible light irradiation [24], considerable progress has been made toward developing the WS_2-containing photocatalyst for H_2 production from water [25–29]. However, their interactions with semiconductors are rarely discussed.

In this paper, WS_2 modified $TiSi_2$ hybrid composite ($WS_2/TiSi_2$) has been successfully fabricated via a two-step method: ultrasonic deposition and postcalcination. Postcalcination at a moderate temperature was found to be effective for forming the heterojunction structure between WS_2 and $TiSi_2$. Compared with $TiSi_2$, the as-prepared $WS_2/TiSi_2$ hybrid exhibited a more negative conduction band level and better photoexcited-charge separation efficiency. The optimal $WS_2/TiSi_2$ composite was proved to be a robust and effective photocatalyst for water-reduction to produce hydrogen under visible light irradiation.

2. Results and Discussion

2.1. Morphology and Structure

For convenience, the prepared catalyst samples were labeled as WS_2-x/$TiSi_2$-y, where x is the weight percentage of WS_2 in the sample and y stands for the calcination temperature. Figure 1 presents the XRD (X-ray diffraction) patterns of WS_2-1/$TiSi_2$ prepared at different calcination temperatures for 2 h. For comparison, the XRD pattern of commercial $TiSi_2$ is also included in the figure. $TiSi_2$ shows characteristic diffraction peaks at 39.2°, 42.3°, 43.2° and 49.8°, corresponding to the (311), (040), (022) and (331) orientations of the orthorhombic structure of $TiSi_2$ (JCPDS: 35-0785) [30]. The X-ray diffraction patterns of the WS_2-1/$TiSi_2$ catalysts prepared at different temperatures demonstrate the same patterns as $TiSi_2$, indicating that the $TiSi_2$ moiety of the catalyst is stable and keeps the orthorhombic structure during the thermal treatment. Interestingly, the intensity of the diffraction peaks increases obviously as the calcination temperature increases, which demonstrates that the thermal-treatment increases the crystallinity of the $TiSi_2$ moiety of the catalyst. However, no diffraction peaks can be assigned to the WS_2 moiety of the catalyst, which may be due to the low content and high dispersity of WS_2 on $TiSi_2$.

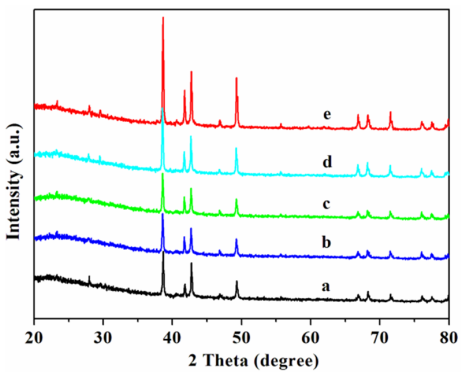

Figure 1. XRD (X-ray diffraction) patterns of (**a**) commercial $TiSi_2$ and WS_2-1/$TiSi_2$ samples prepared at (**b**) 623; (**c**) 673; (**d**) 723; and (**e**) 773 K for 2 h.

Figure 2 shows the SEM images of the commercial $TiSi_2$ and WS_2-1/$TiSi_2$-723. The ball-milled $TiSi_2$ particles exhibit irregular shape with a size in the range of 0.5–2.5 μm (Figure 2A). The morphology of WS_2-1/$TiSi_2$-723 shows almost no change compared with that of $TiSi_2$ and the size of WS_2-1/$TiSi_2$-723 is in the range of 0.5–3 μm (Figure 2B). The elemental distributions of Ti, Si, W and S at the micro scale were determined by SEM-EDX (energy dispersive X-ray spectrometry) mapping and the corresponding results are displayed in Figure 2C–F. From these figures we can see that Ti and Si are the main components of the sample and the content of the W and S elements are much lower than that of Ti and Si, which is ascribed to the low ratio of WS_2 to $TiSi_2$. In addition, it can also be clearly observed that WS_2 is very uniformly dispersed on the surface of the $TiSi_2$ moiety.

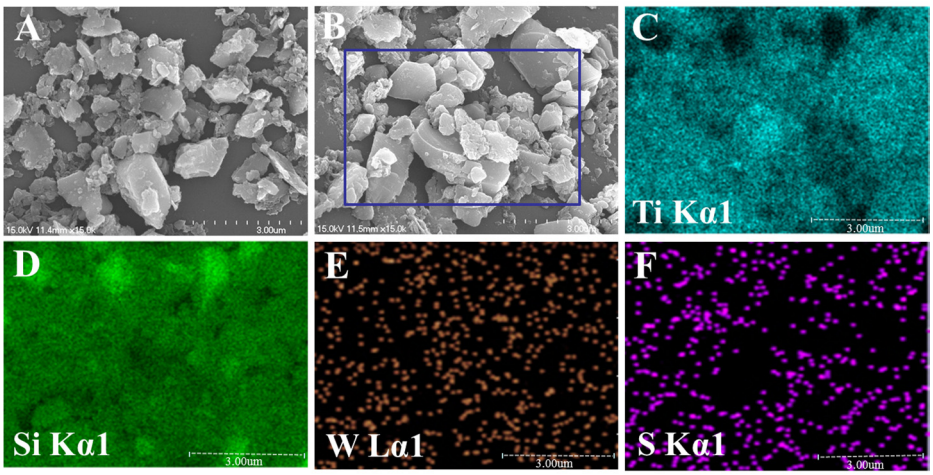

Figure 2. SEM (scanning electron microscopy) images of (**A**) $TiSi_2$ and (**B**) WS_2-1/$TiSi_2$-723; (**C**–**F**) the corresponding EDX (energy dispersive X-ray spectrometry) mapping of the WS_2-1/$TiSi_2$-723 sample at a highlighted region shown in (**B**).

In order to further research the morphology of the samples and the interfacial junction structure between WS_2 and $TiSi_2$, TEM characterization was carried out on $TiSi_2$ and WS_2-1/$TiSi_2$-723. As displayed in Figure 3, the surface of pure $TiSi_2$ is smooth and clear; while for the WS_2-1/$TiSi_2$-723 sample, a layer of rough material is coated on the $TiSi_2$ surface, which indicates that the layered WS_2 particles are intimately covered on the surface of $TiSi_2$.

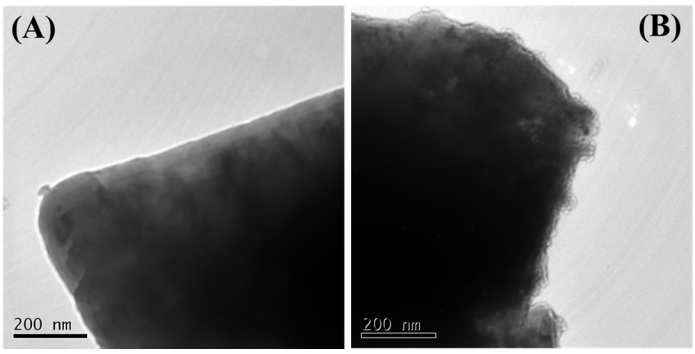

Figure 3. TEM (transmission electron microscopy) images of (**A**) $TiSi_2$ and (**B**) WS_2-1/$TiSi_2$-723.

2.2. TG-DTA (Thermogravimetric-Differential Thermal Analysis) and XPS Analysis

Since WS_2 in the $WS_2/TiSi_2$ composite was converted from the precursor $(NH_4)_2WS_4$, the thermal decomposition behaviour of $(NH_4)_2WS_4$ was investigated by differential thermogravimetry under an N_2 atmosphere. As Figure 4A shows, the thermal decomposition curves of $(NH_4)_2WS_4$, presented as a TG curve, demonstrated two steps of weight loss. The first step of weight loss occurred at 473 K and ended at 573 K. The weight loss at this stage was 17.2%, demonstrating that $(NH_4)_2WS_4$ decomposed to WS_3, NH_3 and H_2S shown as Equation (1) (calc. 19.6 wt %). The intermediate product WS_3 appeared to be stable between 573 K and 623 K. When the sample calcined at higher temperature (>623 K), the second weight loss step occurred, the experimental weight loss for the second step is 9.3%, implying that WS_3 decomposed to WS_2, shown as Equation (2) (calc. 9.2 wt %) [31]. Exceeding 673 K, the slight weight loss can still be observed, mainly due to the sluggish decomposition or condensation of WS_2 at a high temperature.

$$(NH_4)_2WS_4 \rightarrow WS_3 + 2NH_3\uparrow + H_2S\uparrow \quad (1)$$

$$WS_3 \rightarrow WS_2 + S \quad (2)$$

XPS spectra of the WS_2-1/$TiSi_2$ samples calcined at different temperatures are shown in Figure 4B. For both the samples calcined at 473 and 623 K, the W 4f peaks were observed at 35.7 and 37.9 eV, suggesting that tungsten existed as W^{6+} in the samples. When the calcination temperature increased to 673 and 723 K, the W 4f peaks shifted to 32.6 and 34.7 eV, indicating that tungsten transformed from W^{6+} to W^{4+} in the samples [26,32,33]. At a higher calcination temperature (~773 K), the XPS spectrum basically does not change, showing that W species loaded on $TiSi_2$ is stable over a relatively wide temperature range. Combining the results of TG-DTA and XPS, we concluded that $(NH_4)_2WS_4$ loaded on $TiSi_2$ was first decomposed to WS_3 and then to WS_2 in the calcining process (>673 K). The XPS spectrum of the S 2p regions for WS_2-1/$TiSi_2$-723 demonstrated the peaks located at 162.4 and 163.6 eV, confirming that the S element existed as S^{2-} in the sample (Figure S1). The Ti 2p high resolution XPS spectra of $TiSi_2$ and WS_2-1/$TiSi_2$-723 are shown in Figure 4C. For the $TiSi_2$ sample, the weak peak centred at 453.1 eV belongs to Ti^0 $2p_{3/2}$, indicating that trace metallic Ti exists on the surface of $TiSi_2$. The other two strong peaks, centred at 458.95 and 464.75 eV, could be ascribed to Ti^{4+} $2p_{3/2}$ and $2p_{1/2}$, respectively, demonstrating that the surface layer of $TiSi_2$ in the depth of XPS measurement (ca. 2.5–10 nm) is highly oxidized [14,15]. For the WS_2-1/$TiSi_2$-723 catalyst, the binding energy of Ti^{4+} 2p shifts slightly to the higher energy and the peak of Ti^0 $2p_{3/2}$ disappeared, indicating that the Ti metal in the surface of Ti-Si has been oxidized in the pyrolysis process. Si 2p high resolution XPS spectra of $TiSi_2$ and WS_2-1/$TiSi_2$-723 are shown in Figure 4D. The $TiSi_2$ sample shows two peaks centred at 98.65 and 102.59 eV, corresponding to Si^0 $2p_{3/2}$ and Si^{4+} $2p_{1/2}$, respectively [14]. The positive shift of the binding energies of Si^0 $2p_{3/2}$ and Si^{4+} $2p_{1/2}$ in WS_2-1/$TiSi_2$-723 was also observed. Meanwhile, the intensity of the peak corresponding to Si^0 $2p_{3/2}$ decreased greatly in WS_2-1/$TiSi_2$-723. The shifts of the binding energies of both Ti and Si indicate that some kind of chemical bonds, such as Ti-S-W and Si-S-W, might have formed at the interface of the $TiSi_2$ and WS_2 components.

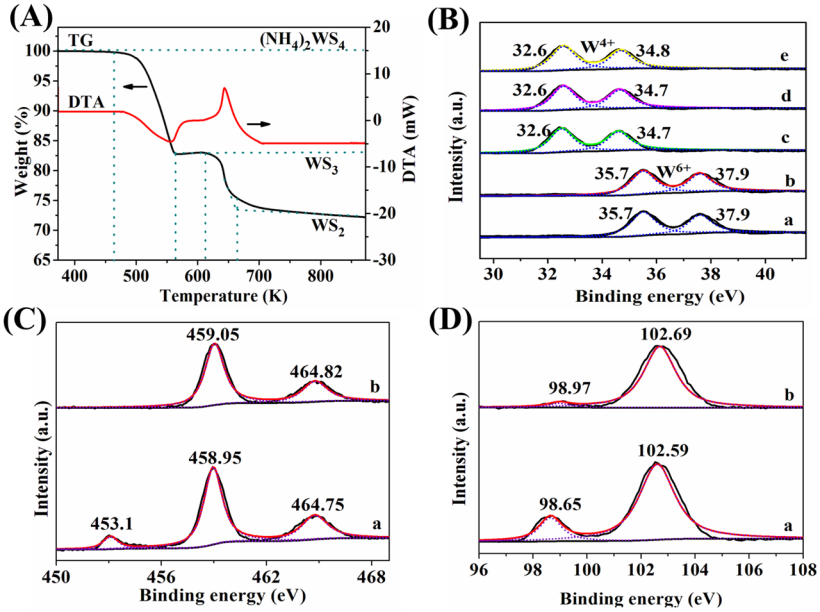

Figure 4. (**A**) TG-TDA (thermogravimetric-differential thermal analysis) curves of the decomposition of $(NH_4)_2WS_4$; (**B**) XPS spectra of the W 4f regions for WS_2-1/$TiSi_2$ calcined at (a) 473, (b) 623, (c) 673, (d) 723 and (e) 773 K for 2 h; (**C**) High-resolution XPS (X-ray photoelectron spectroscopy) spectra of Ti 2p in (a) $TiSi_2$ and (b) WS_2-1/$TiSi_2$-723; (**D**) High-resolution XPS spectra of Si 2p in (a) $TiSi_2$ and (b) WS_2-1/$TiSi_2$-723.

2.3. Optical and Photoelectrochemical Properties

The results of the linear sweep voltammetry (LSV) for $TiSi_2$ and WS_2-1/$TiSi_2$-723 electrodes are displayed in Figure 5A. The proton reduction potential of the $TiSi_2$ electrode is ca. −0.20 V vs. RHE (reversible hydrogen electrode), but it changes to −0.13 V vs. RHE for the WS_2-1/$TiSi_2$-723 electrode, indicating that the introduction of WS_2 can reduce the hydrogen evolution potential [34,35], which is a property that is usually demonstrated by the noble metal nanoparticles such as Pt [36]. The replacement of Pt by WS_2 apparently can offer an opportunity to create an inexpensive photocatalyst system for H_2 evolution. In order to further investigate the role of WS_2, the flat band potentials of the $TiSi_2$ and WS_2-1/$TiSi_2$-723 electrodes were measured respectively. The flat band potential (E_{fb}) was determined by the onset potential of the Mott-Schottky (M-S) plots [37]. As demonstrated in Figure 5B, both $TiSi_2$ and WS_2-1/$TiSi_2$-723 electrodes exhibit a positive slope, indicating an n-type semiconductor feature [38]. The E_{fb} of the $TiSi_2$ electrode estimated from the x intercepts of the linear region of the MS plot is ca. −0.39 V vs. RHE, while it is ca. −0.77 V vs. RHE for the WS_2-1/$TiSi_2$-723 electrode. The results show that combining of $TiSi_2$ and WS_2 may shift the flat potential of the composite to a more negative position. Since the flat band potential of an n-type semiconductor may be considered approximately as the conduction band edge, the shift of the flat potential of the composite indicates that WS_2-1/$TiSi_2$-723 has a higher electron donor level, which is beneficial for water reduction.

The optical band gap of semiconductors was determined by the Tauc equation [39]:

$$(\alpha h\nu)^n = A(h\nu - E_g)$$

where α is the measured absorption coefficient, $h\nu$ is the photon energy, A and n are constant, and E_g is the optical band gap energy. The value of n is 0.5 and 2 for the indirect and direct band gap, respectively. Since both $TiSi_2$ and WS_2 have a direct band gap, the value of n is 2. E_g is estimated by the intercept of the photon energy axis, obtained by extrapolating the linear region of the plot [40]. The Tauc plots (Figure 5C,D) show that the optical band gaps are 2.41 for $TiSi_2$ and 2.15 eV for WS_2-1/$TiSi_2$-723. The decrease of the optical band gap of WS_2-1/$TiSi_2$-723, which may be attributed to the interaction

between $TiSi_2$ and WS_2, is beneficial for the composite photocatalyst to respond to the visible light in a wider range. From the discussion above, we can estimate the band levels of pure $TiSi_2$ (E_{VB} = 2.02, E_C = −0.39 V vs. RHE) and the WS_2-1/$TiSi_2$-723 composite (E_{VB} = 1.38, E_{CB} = −0.77 V vs. RHE). The variation of the bandgap and the band edges indicates the strong interaction between $TiSi_2$ and WS_2 moieties, mostly occurred at the surface.

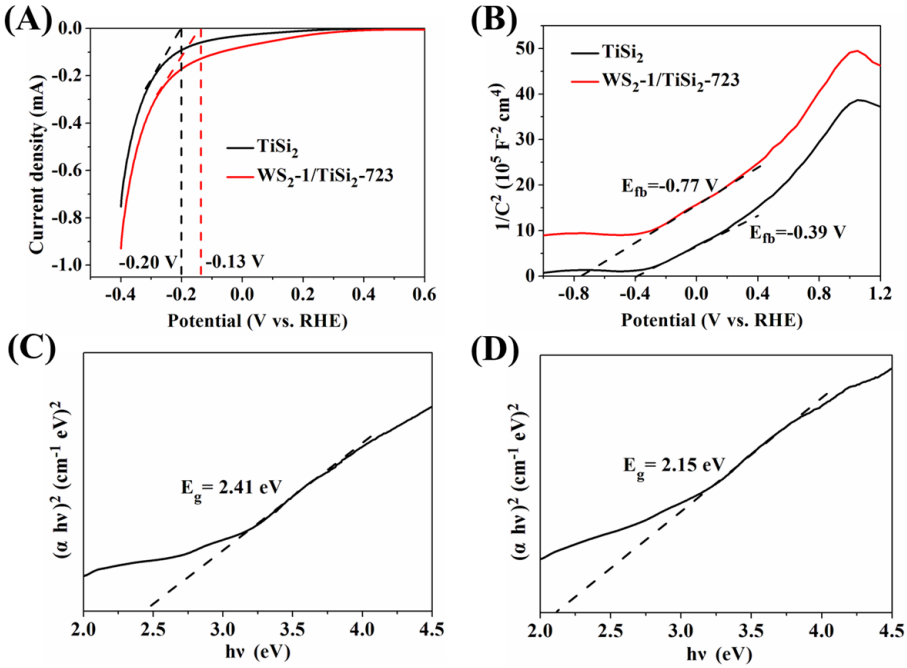

Figure 5. (**A**) The linear sweep voltammetry plots of the $TiSi_2$ and WS_2-1/$TiSi_2$-723 electrodes scanning from −1.0 to 0 V vs. SCE (saturated calomel electrode) with a scan rate of 50 mV·s^{-1}, the proton reduction potential at 0 mA is −0.20 V for $TiSi_2$ and −0.13 V for WS_2-1/$TiSi_2$-723; (**B**) the Mott-Schottky plots of the $TiSi_2$ and WS_2-1/$TiSi_2$-723 electrodes. Tauc plots of (**C**) $TiSi_2$ and (**D**) WS_2-1/$TiSi_2$-723.

It is well known that the photoluminescence (PL) spectroscopy could be useful to reveal the photo-generated charge transfer process. The PL spectra of $TiSi_2$ and WS_2-1/$TiSi_2$-723 excited at 532 nm are shown in Figure S2. Both $TiSi_2$ and WS_2-1/$TiSi_2$-723 display an emission peak centred at 600 nm, however, the PL intensity of WS_2-1/$TiSi_2$-723 is much lower than that of $TiSi_2$ and the calculated quenching efficiency for WS_2-1/$TiSi_2$-723 is 43.6%, indicating an efficient photoexcited electron transfer from $TiSi_2$ to WS_2.

A photoelectrochemical study was conducted to investigate the photoinduced charge separation and transfer processes at the electrode interface. As shown in Figure 6A, a prompt and reversible photocurrent response can be observed from both the $TiSi_2$ and WS_2-1/$TiSi_2$-723 electrode under chopped light irradiation. The WS_2-1/$TiSi_2$-723 electrode shows higher photocurrent density than pure $TiSi_2$, indicating that formation of the heterojunction structure in WS_2-1/$TiSi_2$-723 results in better charge separation, as well as excellent incident light harvesting. Figure 6B shows the electrochemical impedance spectra (EIS) of $TiSi_2$ and WS_2-1/$TiSi_2$-723 electrodes presented as Nyquist plots. The radius of the plot of WS_2-1/$TiSi_2$-723 is much smaller than that of $TiSi_2$. The fact demonstrates that the charge transfer resistance is significantly decreased on the WS_2-1/$TiSi_2$-723 interface [41,42], which is in agreement with the results of photocurrent responses measurements. The transfer resistance decreases, so the rate of charge separation is accelerated, and the photocurrent is enhanced.

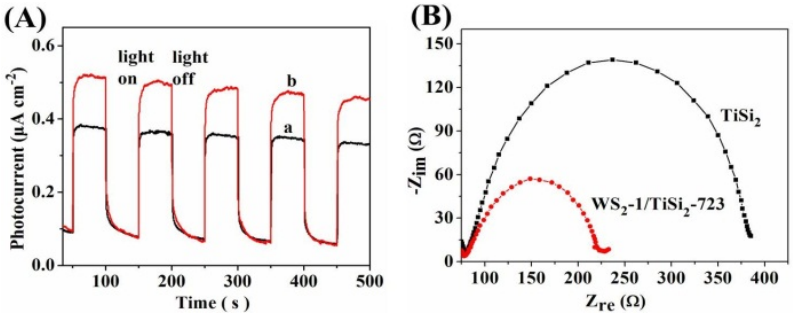

Figure 6. (**A**) Photocurrent of the electrodes made of (a) $TiSi_2$ and (b) WS_2-1/$TiSi_2$-723 catalysts under UV-vis light irradiation at 0.5 V vs. SCE. The electrolyte was 0.5 M Na_2SO_4 aqueous solution. The illumination from a 150 W xenon lamp was interrupted every 50 s; (**B**) Nyquist plots of electrochemical impedance spectra (EIS) for $TiSi_2$ and WS_2-1/$TiSi_2$-723 in 5.0 mM $K_3[Fe(CN)_6]/K_2[Fe(CN)_6]$ (1:1) aqueous solution at a potential of 0.2 V vs. SCE.

2.4. Photocatalytic Hydrogen Evolution

Firstly, the influence of calcination temperature on H_2 evolution rate of the WS_2-1/$TiSi_2$ sample was investigated. Figure 7A shows the influence of the catalysts calcined at different temperatures from 623 to 773 K on the rate of H_2 evolution. With the increase of the calcination temperature, the H_2 evolution rate of the catalyst increases gradually. The maximum H_2 evolution rate was obtained from the WS_2-1/$TiSi_2$-723 catalyst (99.4 μmol·h^{-1}·g^{-1}). However, further increasing the calcination temperature, the rate of H_2 evolution decreases instead. As discussed above, 623 K is the temperature starting to form WS_2, and 773 K is the temperature at which WS_2 gets stabilized. The influence of calcination temperature may be attributed to the fact that the catalyst calcined at proper temperature may strengthen the junction formation between $TiSi_2$ and WS_2, which is beneficial for the photocatalytic activity of the catalyst. However, higher calcination temperature may cause the surface areas of the catalyst to decrease or even the formed heterojunction to collapse, resulting in a photocatalytic efficiency decrease. Figure 7B shows the influence of the ratio of $TiSi_2$ and WS_2 of the composite catalyst on the photocatalytic activity. For comparison, the photocatalytic results of pure $TiSi_2$ and 1 wt % Pt modified $TiSi_2$ (Pt-1/$TiSi_2$) are also included in the figure. The catalyst loading with ca. 1 wt % WS_2 demonstrated the highest photocatalytic activity among all WS_2/$TiSi_2$-723 catalysts with various WS_2 loading. In 6 h visible light irradiation, WS_2-1/$TiSi_2$-723 produced about 596.4 μmol·g^{-1} hydrogen, which was even higher than that of Pt-1/$TiSi_2$ (532.9 μmol·g^{-1}). However, further loading of WS_2 on $TiSi_2$ led to a catalytic efficiency decrease, which may be attributed to the fact that the excess WS_2 on $TiSi_2$ may produce a light shading effect or introduce charge recombination sites [27]. The similar phenomena were also found in several other photocatalyst composites [21,34].

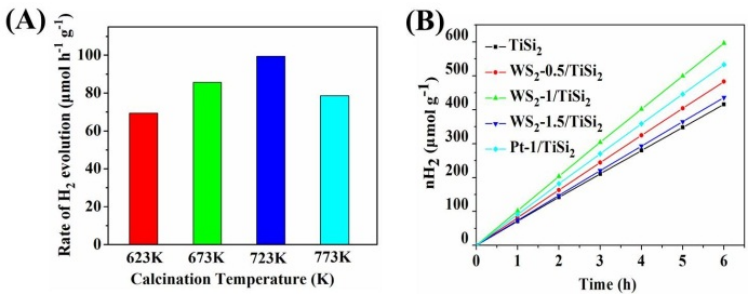

Figure 7. (**A**) The H_2 evolution rates of WS_2-1/$TiSi_2$-*y* catalysts prepared at different temperatures; (**B**) the hydrogen production of $TiSi_2$, WS_2-*x*/$TiSi_2$-723, and Pt-1/$TiSi_2$ catalysts over 6 h. Reaction conditions: 50 mg catalysts, 60 mL 0.005 M oxalic acid aqueous solution, irradiation source: a 150 W Xe lamp equipped with a cut-off filter at 420 nm.

The stability of the WS_2-1/$TiSi_2$-723 catalyst was estimated by performing recycling photocatalytic experiments and the results are shown in Figure 8. For comparison, the stability of pure $TiSi_2$ was also estimated under the same reaction conditions. After 6 h of visible light irradiation, $TiSi_2$ produced ca. 416.0 μmol·g^{-1} H_2 in the first cycle, while WS_2-1/$TiSi_2$-723 produced ca. 596.4 μmol·g^{-1} H_2. Both activities of $TiSi_2$ and WS_2-1/$TiSi_2$-723 were slightly reduced (348.5 μmol·g^{-1} and 525.6 μmol·g^{-1}) in the second cycle. In the next three cycles, the amount of H_2 produced from $TiSi_2$ was still reduced, which was mainly due to the surface oxidation of $TiSi_2$ [14,43]. On the other hand, the amount of H_2 produced from WS_2-1/$TiSi_2$-723 was basically unchanged. The above results demonstrate that the WS_2/$TiSi_2$ photocatalyst might be a promising candidate for photocatalytic water reduction to produce hydrogen under solar-light irradiation since it possesses higher photocatalytic activity, higher stability and lower fabrication cost.

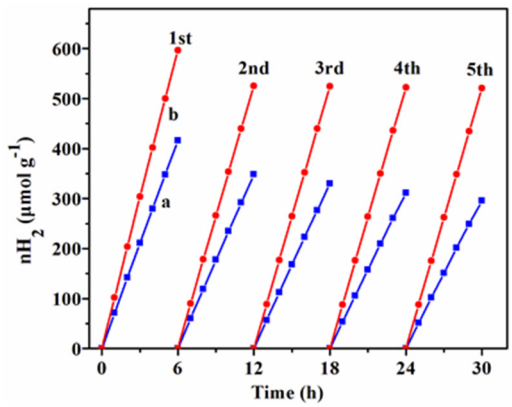

Figure 8. The recycling photocatalytic experiments of (a) $TiSi_2$ and (b) WS_2-1/$TiSi_2$-723. Reaction conditions: 50 mg catalysts, 60 mL 0.005 M oxalic acid aqueous solution, a 150 W Xe lamp equipped with a cut-off filter at 420 nm.

The proposed mechanism of photocatalytic H_2 evolution on the WS_2/$TiSi_2$ catalyst is shown in Scheme 1. Under visible-light irradiation, the electrons in the valence band (VB) of $TiSi_2$ are stimulated to the conduction band (CB). Then, the photo-generated electrons transfer from the conduction band of $TiSi_2$ to the WS_2, where H^+ is reduced to hydrogen. The holes that remained on the valence band of $TiSi_2$ transfer to the surface and react with the oxalic acid in the solution. This process efficiently inhibits the photo-generated charges recombination, and significantly enhances the photocatalytic hydrogen evolution efficiency.

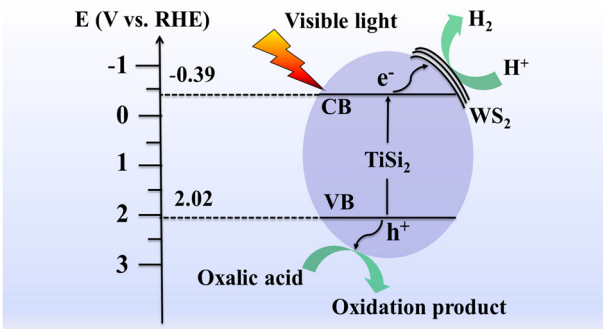

Scheme 1. A schematic illustration of the charge transfer for hydrogen evolution over the WS_2-x/$TiSi_2$-y photocatalyst under visible light irradiation.

3. Materials and Methods

3.1. Synthesis

$TiSi_2$ was purchased from the J&K Company (Shanghai, China) and other chemical reagents were purchased from the Sinopharm Chemical Reagent Company (Shanghai, China). The commercial $TiSi_2$ powder was ball-milled for 4 h at the speed of 210 rpm (rotation per minute) in advance and other chemicals were used without further purification.

Ammonium tetrathiotungstate ($(NH_4)_2WS_4$) was prepared using the method described in the literature [44]. In a typical experiment, 5 g of ammonium tungstate was dispersed in a 50 mL NH_3 aqueous solution (6 M). H_2S gas was then bubbled into the above dispersed solution at 333 K for 4 h. After being cooled to room temperature, the reaction solution was put into a refrigerator and maintained at 278 K overnight. The precipitate of orange-yellow $(NH_4)_2WS_4$ crystals was isolated by filtration, rinsed with isopropanol and dried under vacuum.

The $WS_2/TiSi_2$ photocatalyst was prepared by ultrasonic deposition combined with postpyrolysis method. $(NH_4)_2WS_4$ aqueous solution was mixed with the ball-milled $TiSi_2$ powder under magnetic stirring, and then the mixture was ultra-sonicated for 5 h. The resulting $(NH_4)_2WS_4/TiSi_2$ precursor was dried in a vacuum oven at 323 K. Finally, the solid powder was calcined in Ar atmosphere at different temperatures in the range from 473 to 773 K for 2 h, resulting in WS_2 modified $TiSi_2$ photocatalyst, in which the content of WS_2 could be adjusted by tuning the weight ratio of the precursors of $(NH_4)_2WS_4$ and $TiSi_2$. According to the decomposition process of $(NH_4)_2WS_4$, the weight percentage of WS_2 in the sample was calculated by supposing that the $(NH_4)_2WS_4$ was completely converted to WS_2.

3.2. Characterization

X-ray powder diffraction (XRD) measurements were carried out on a Philips diffractometer (X'Pert-Pro MRD, Amsterdam, Netherland) using Ni-filtered Cu Kα radiation in the range 20°–80° (2θ). Scanning electron microscopy (SEM) and Energy dispersive X-ray spectrometry (EDX) mapping measurements were taken on a Hitachi S-4700 microscope (Hitachi Corporation, Tokyo, Japan). Transmission electron microscopy (TEM) studies were conducted using a transmission electron microscope (JEOL JEM-2100, JEOL Ltd., Tokyo, Japan) operating at an accelerating voltage of 200 kV. TG-TDA curves of the decomposition of $(NH_4)_2WS_4$ were recorded by using differential thermal analysis/thermogravimetric equipment under a N_2 flow with the heating rate of 10 K/min. X-ray photoelectron spectroscopy (XPS) of the samples was taken on a Thermo Scientific ESCALA 250Xi XPS spectrometer (Kratos Analytical Ltd., Manchester, UK). Room temperature UV-vis diffuse reflectance absorption spectra (DRS) were measured on a UV-1800 SPC spectrophotometer (Shimadzu, Kyoto, Japan). Photoluminescence (PL) spectra of the samples were recorded on an Edinburgh PLS920 fluorospectrophotometer (Edinburgh Instruments Ltd., Edinburgh, UK).

3.3. Photoelectrochemical Measurements

The measurements of photoelectrochemical properties of the samples were performed by dipping a clean indium tin oxide (ITO) glass (1 × 2.5 cm) into the ethanol suspension of the relative catalyst several times and drying under a vacuum at 323 K as a working electrode. The measurements were carried out on a CHI 660D potentiostat/galvanostat electrochemical analyser (CH Instruments Inc, Shanghai, China) in a three-electrode system consisting of the working electrode, a saturated calomel electrode (SCE) as a reference electrode and a platinum wire as a counter electrode. The electrodes were immersed in a 0.5 M Na_2SO_4 aqueous solution (pH ~6). During the measurement, the working electrode was irradiated by a GY-10 xenon lamp (150 W, Tian Jin Tuo Pu Instruments Co., Ltd, Tianjin, China). The electrochemical impedance spectra (EIS), displayed as a Nyquist plot, were carried out in the similar system except that the electrodes were immersed in a 5.0 mM solution

of $K_3[Fe(CN)_6]/K_2[Fe(CN)_6]$ (1:1). The Mott-Schottky (M-S) plots were measured with a frequency of 1000 Hz.

3.4. Photocatalytic Reaction

The photocatalytic reaction was carried out in a 70 mL quartz flask equipped with a flat optical entry window. In a typical photocatalytic experiment, 50 mg of the as-prepared photocatalyst and 60 mL of oxalic acid aqueous solution (0.005 M) were added into the quartz flask whilst stirring [45]. The system was deaerated by bubbling argon into the solution for 30 min before the reaction. A 150 W xenon lamp with a 420 nm cut-off filter was used as the visible light source. The lamp was positioned ca. 10 cm away from the optical entry window of the reactor. The produced hydrogen gas was analysed with an online gas chromatograph (GC1650) equipped with a thermal conductivity detector (TCD) (Ke Xiao Instruments Co., Ltd, Hangzhou, China) and 5 Å molecular sieve columns using argon as the carrier gas. The standard H_2-Ar gas mixtures of known concentrations were used for GC signal calibration.

4. Conclusions

In summary, a novel $WS_2/TiSi_2$ hybrid composite has been successfully synthesized and used for photocatalytic hydrogen evolution. The photocatalytic activity of $TiSi_2$ under visible light ($\lambda > 420$ nm) irradiation can be enhanced by loading WS_2 as a cocatalyst, and the activity of optimal $WS_2/TiSi_2$ composite is even higher than that of platinized $TiSi_2$ under the same reaction conditions. The junction formed between $TiSi_2$ and surface WS_2, together with the excellent H_2 evolution property of WS_2, is supposed to be responsible for the enhanced photocatalytic activity of the $WS_2/TiSi_2$ composite catalyst. This study shows a paradigm of developing the eco-friendly, cost-effective photocatalyst for hydrogen production from water.

Supplementary Materials: The following are available online at www.mdpi.com/2073-4344/6/9/136/s1, Figure S1: XPS (X-ray photoelectron spectroscopy) spectrum of the S 2p regions for the WS_2-1/$TiSi_2$-723 sample. (The blue lines: the deconvolved peaks for S 2p3/2 and S 2p1/2 of WS_2-1/TiSi2-723; the red line: the fitted result of the blue lines.). Figure S2: Photoluminescence spectra of $TiSi_2$ and WS_2-1/$TiSi_2$-723. Excited wavelength: 532 nm.

Acknowledgments: The authors gratefully acknowledge financial support of this research by the National Natural Science Foundation of China (21373143) and the Priority Academic Program Development of Jiangsu Higher Education Institutions (PAPD).

Author Contributions: The manuscript was written through contributions of all authors. All authors have given approval to the final version of the manuscript.

Conflicts of Interest: The authors declare no competing financial interest.

References

1. Gratzel, M. Photoelectrochemical cells. *Nature* **2001**, *414*, 338–344. [CrossRef] [PubMed]
2. Sato, J.; Kobayashi, H.; Ikarashi, K.; Saito, N.; Nishiyama, H.; Inoue, Y. Photocatalytic Activity for Water Decomposition of RuO_2-Dispersed Zn_2GeO_4 with d^{10} Configuration. *J. Phys. Chem. B* **2004**, *108*, 4369–4375. [CrossRef]
3. Ingler, W.B.; Baltrus, J.P.; Khan, S.U.M. Photoresponse of p-Type Zinc-Doped Iron(III) Oxide Thin Films. *J. Am. Chem. Soc.* **2004**, *126*, 10238–10239. [CrossRef] [PubMed]
4. Liao, C.-H.; Huang, C.-W.; Wu, J.C.S. Hydrogen Production from Semiconductor-based Photocatalysis via Water Splitting. *Catalysts* **2012**, *2*, 490–516. [CrossRef]
5. Lin, Y.J.; Xu, Y.; Mayer, M.T.; Simpson, Z.I.; McMahon, G.; Zhou, S.; Wang, D.W. Growth of p-Type Hematite by Atomic Layer Deposition and Its Utilization for Improved Solar Water Splitting. *J. Am. Chem. Soc.* **2012**, *134*, 5508–5511. [CrossRef] [PubMed]
6. Mishra, G.; Parida, K.M.; Singh, S.K. Facile Fabrication of S-TiO_2/β-SiC Nanocomposite Photocatalyst for Hydrogen Evolution under Visible Light Irradiation. *ACS Sustain. Chem. Eng.* **2015**, *3*, 245–253. [CrossRef]
7. Fujishima, A.; Honda, K. Electrochemical Photolysis of Water at a Semiconductor Electrode. *Nature* **1972**, *238*, 37–38. [CrossRef] [PubMed]

8. Woan, K.; Pyrgiotakis, G.; Sigmund, W. Photocatalytic Carbon-Nanotube—TiO_2 Composites. *Adv. Mater.* **2009**, *21*, 2233–2239. [CrossRef]
9. Yang, P.; Lu, C.; Hua, N.P.; Du, Y.K. Titanium dioxide nanoparticles co-doped with Fe^{3+} and Eu^{3+} ions for photocatalysis. *Mater. Lett.* **2002**, *57*, 794–801. [CrossRef]
10. Maeda, K.; Takata, T.; Hara, M.; Saito, N.; Inoue, Y.; Kobayashi, H.; Domen, K. GaN:ZnO Solid Solution as a Photocatalyst for Visible-Light-Driven Overall Water Splitting. *J. Am. Chem. Soc.* **2005**, *127*, 8286–8287. [CrossRef] [PubMed]
11. Pany, S.; Parida, K.M. Sulfate-Anchored Hierarchical Meso-Macroporous N-doped TiO_2: A Novel Photocatalyst for Visible Light H_2 Evolution. *ACS Sustain. Chem. Eng.* **2014**, *2*, 1429–1438. [CrossRef]
12. Liu, J.; Liu, Y.; Liu, N.Y.; Han, Y.Z.; Zhang, X.; Huang, H.; Lifshitz, Y.; Lee, S.-T.; Zhong, J.; Kang, Z.H. Metal-free efficient photocatalyst for stable visible water splitting via a two-electron pathway. *Science* **2015**, *347*, 970–974. [CrossRef] [PubMed]
13. Tedesco, J.L.; Rowe, J.E.; Nemanich, R.J. Titanium silicide islands on atomically clean Si(100): Identifying single electron tunneling effects. *J. Appl. Phys.* **2010**, *107*, 123715. [CrossRef]
14. Ritterskamp, P.; Kuklya, A.; Wüstkamp, M.-A.; Kerpen, K.; Weidenthaler, C.; Demuth, M. A Titanium Disilicide Derived Semiconducting Catalyst for Water Splitting under Solar Radiation—Reversible Storage of Oxygen and Hydrogen. *Angew. Chem. Int. Ed.* **2007**, *46*, 7770–7774. [CrossRef] [PubMed]
15. Mou, Z.G.; Yin, S.L.; Zhu, M.S.; Wang, X.M.; Zheng, J.W.; Lu, C.; Du, Y.K.; Yang, P. $RuO_2/TiSi_2$/graphene composite for enhanced photocatalytic hydrogen generation under visible light irradiation. *Phys. Chem. Chem. Phys.* **2013**, *15*, 2793–2799. [CrossRef] [PubMed]
16. Lingampalli, S.R.; Gautam, U.K.; Rao, C.N.R. Highly efficient photocatalytic hydrogen generation by solution-processed ZnO/Pt/CdS, ZnO/Pt/$Cd_{1-x}Zn_xS$ and ZnO/Pt/$CdS_{1-x}Se_x$ hybrid nanostructures. *Energy Environ. Sci.* **2013**, *6*, 3589–3594. [CrossRef]
17. Wang, Y.B.; Wang, Y.S.; Xu, R. Photochemical Deposition of Pt on CdS for H_2 Evolution from Water: Markedly Enhanced Activity by Controlling Pt Reduction Environment. *J. Phys. Chem. C* **2013**, *117*, 783–790. [CrossRef]
18. Zhang, Z.J.; Lu, Z-H.; Chen, X.S. Ultrafine Ni-Pt Alloy Nanoparticles Grown on Graphene as Highly Efficient Catalyst for Complete Hydrogen Generation from Hydrazine Borane. *ACS Sustain. Chem. Eng.* **2015**, *3*, 1255–1261. [CrossRef]
19. Zong, X.; Yan, H.J.; Wu, G.P.; Ma, G.J.; Wen, F.Y.; Wang, L.; Li, C. Enhancement of Photocatalytic H_2 Evolution on CdS by Loading MoS_2 as Cocatalyst under Visible Light Irradiation. *J. Am. Chem. Soc.* **2008**, *130*, 7176–7177. [CrossRef] [PubMed]
20. Liu, Y.Y.; Xie, S.F.; Li, H.; Wang, X.Y. A Highly Efficient Sunlight Driven ZnO Nanosheet Photocatalyst: Synergetic Effect of P-Doping and MoS_2 Atomic Layer Loading. *ChemCatChem* **2014**, *6*, 2522–2526. [CrossRef]
21. Chen, G.P.; Li, D.M.; Li, F.; Fan, Y.Z.; Zhao, H.F.; Luo, Y.H.; Yu, R.C.; Meng, Q.B. Ball-milling combined calcination synthesis of MoS_2/CdS photocatalysts for high photocatalytic H_2 evolution activity under visible light irradiation. *Appl. Catal. A Gen.* **2012**, *443*, 138–144. [CrossRef]
22. Xiang, Q.J.; Yu, J.G.; Jaroniec, M. Synergetic Effect of MoS_2 and Graphene as Cocatalysts for Enhanced Photocatalytic H_2 Production Activity of TiO_2 Nanoparticles. *J. Am. Chem. Soc.* **2012**, *134*, 6575–6578. [CrossRef] [PubMed]
23. Lu, Y.T.; Wang, D.D.; Yang, P.; Du, Y.K.; Lu, C. Coupling $Zn_xCd_{1-x}S$ nanoparticles with graphenelike MoS_2: Superior interfacial contact, low overpotential and enhanced photocatalytic activity under visible-light irradiation. *Catal. Sci. Technol.* **2014**, *4*, 2650–2657. [CrossRef]
24. Jing, D.W.; Guo, L.J. WS_2 sensitized mesoporous TiO_2 for efficient photocatalytic hydrogen production from water under visible light irradiation. *Catal. Commun.* **2007**, *8*, 795–799. [CrossRef]
25. Zong, X.; Han, J.F.; Ma, G.J.; Yan, H.J.; Wu, G.P.; Li, C. Photocatalytic H_2 Evolution on CdS Loaded with WS_2 as Cocatalyst under Visible Light Irradiation. *J. Phys. Chem. C* **2011**, *115*, 12202–12208. [CrossRef]
26. Wu, Z.Z.; Fang, B.Z.; Bonakdarpour, A.; Sun, A.K.; Wilkinson, D.P.; Wang, D.Z. WS_2 nanosheets as a highly efficient electrocatalyst for hydrogen evolution reaction. *Appl. Catal. B Environ.* **2012**, *125*, 59–66. [CrossRef]
27. Chen, G.P.; Li, F.; Fan, Y.Z.; Luo, Y.H.; Li, D.M.; Meng, Q.B. A novel noble metal-free ZnS-WS_2/CdS composite photocatalyst for H_2 evolution under visible light irradiation. *Catal. Commun.* **2013**, *40*, 51–54. [CrossRef]
28. Cheng, L.; Huang, W.J.; Gong, Q.F.; Liu, C.H.; Liu, Z.; Li, Y.G.; Dai, H.J. Ultrathin WS_2 Nanoflakes as a High-Performance Electrocatalyst for the Hydrogen Evolution Reaction. *Angew. Chem. Int. Ed.* **2014**, *53*, 7860–7863. [CrossRef] [PubMed]

29. Adriano, A.; Zdenêk, S.; Martin, P. 2H→1T phase transition and hydrogen evolution activity of MoS_2, $MoSe_2$, WS_2 and WSe_2 strongly depends on the MX_2 composition. *Chem. Commun.* **2015**, *51*, 8450–8453.
30. Yen, B.K. X-ray diffraction study of solid-state formation of metastable $MoSi_2$ and $TiSi_2$ during mechanical alloying. *J. Appl. Phys.* **1997**, *81*, 7061–7063. [CrossRef]
31. An, G.J.; Chai, Y.M.; Zhong, H.J.; Zhang, C.F.; Liu, C.G. Thermal decompositon behavior of ammonium tertrathiotungstate under nitrogen atmosphere. *Abstr. Pap. Am. Chem. Soc.* **2005**, *230*, U2321–U2322.
32. Bhandavat, R.; David, L.; Singh, G. Synthesis of Surface-Functionalized WS_2 Nanosheets and Performance as Li-ion Battery Anodes. *J. Phys. Chem. Lett.* **2012**, *3*, 1523–1530. [CrossRef] [PubMed]
33. Zou, J.-P.; Ma, J.; Luo, J.-M.; Yu, J.; He, J.K.; Meng, Y.T.; Luo, Z.; Bao, S.-K.; Liu, H.-L.; Luo, S.-L.; et al. Fabrication of novel heterostructured few layered WS_2-Bi_2WO_6/$Bi_{3.84}W_{0.16}O_{6.24}$ composites with enhanced photocatalytic performance. *Appl. Catal. B* **2015**, *179*, 220–228. [CrossRef]
34. Frame, F.A.; Osterloh, F.E. CdSe-MoS_2: A Quantum Size-Confined Photocatalyst for Hydrogen Evolution from Water under Visible Light. *J. Phys. Chem. C* **2010**, *114*, 10628–10633. [CrossRef]
35. Meng, F.K.; Li, J.T.; Cushing, S.K.; Zhi, M.J.; Wu, N.Q. Solar Hydrogen Generation by Nanoscale p-n Junction of p-type Molybdenum Disulfide/n-type Nitrogen-Doped Reduced Graphene Oxide. *J. Am. Chem. Soc.* **2013**, *135*, 10286–10289. [CrossRef] [PubMed]
36. Huang, Q.; Li, Q.; Xiao, X.D. Hydrogen Evolution from Pt Nanoparticles Covered p-Type CdS:Cu Photocathode in Scavenger-Free Electrolyte. *J. Phys. Chem. C* **2014**, *118*, 2306–2311. [CrossRef]
37. Cardo, F.; Gomes, W.P. On the determination of the flat-band potential of a semiconductor in contact with a metal or an electrolyte from the Mott-Schottky plot. *J. Phys. D Appl. Phys.* **1978**, *11*, L63–L67. [CrossRef]
38. Zhang, L.-W.; Fu, H.-B.; Zhu, Y.-F. Efficient TiO_2 Photocatalysts from Surface Hybridization of TiO_2 Particles with Graphite-like Carbon. *Adv. Funct. Mater.* **2008**, *18*, 2180–2189. [CrossRef]
39. Kaneka, H.; Nishimoto, S.; Miyake, K.; Suedomi, N. Physical and electrochemichromic properties of rf sputtered tungsten oxide films. *J. Appl. Phys.* **1986**, *59*, 2526–2534. [CrossRef]
40. Al-Gaashani, R.; Radiman, S.; Tabet, N.; Daud, A.R. Rapid synthesis and optical properties of hematite (α-Fe_2O_3) nanostructures using a simple thermal decomposition method. *J. Alloys Compd.* **2013**, *550*, 395–401. [CrossRef]
41. Park, Y.; Kang, S.-H.; Choi, W.Y. Exfoliated and reorganized graphite oxide on titania nanoparticles as an auxiliary co-catalyst for photocatalytic solar conversion. *Phys. Chem. Chem. Phys.* **2011**, *13*, 9425–9431. [CrossRef] [PubMed]
42. He, B.-L.; Dong, B.; Li, H.-L. Preparation and electrochemical properties of Ag-modified TiO_2 nanotube anode material for lithium-ion battery. *Electrochem. Commun.* **2007**, *9*, 425–430. [CrossRef]
43. Li, Q.Y.; Lu, G.X. Significant Effect of Pressure on the H_2 Releasing from Photothermal-Catalytic Water Steam Splitting over $TiSi_2$ and Pt/TiO_2. *Catal. Lett.* **2008**, *125*, 376–379. [CrossRef]
44. Thomazeau, C.; Geantet, C.; Lacroix, M.; Harle, V.; Benazeth, S.; Marhic, C.; Danot, M. Two Cation Disulfide Layers in the $W_xMo_{(1-x)}S_2$ Lamellar Solid Solution. *J. Solid State Chem.* **2001**, *160*, 147–155. [CrossRef]
45. Liu, J.J.; Bai, Y.N.; Chen, P.W.; Cui, N.F.; Yin, H. Reaction synthesis of $TiSi_2$ and Ti_5Si_3 by ball-milling and shock loading and their photocatalytic activities. *J. Alloys Compd.* **2013**, *555*, 375–380. [CrossRef]